

**A method for determining venous contribution to
BOLD contrast sensory activation.**

* Deborah A Hall ^{CA}, * Miguel S. Gonçalves,
‡ Steve Smith, ‡ Peter Jezzard, * Mark P. Haggard, * John Kornak.

* MRC Institute of Hearing Research,
University Park,
Nottingham,
UK.
NG7 2RD

‡ The Oxford Centre for Functional Magnetic Resonance Imaging of the Brain
(fMRIB),
John Radcliffe Hospital,
Headington,
Oxford,
UK.
OX3 9DU

^{CA} corresponding author
Tel: (+44) 115 922 3431
Fax: (+44) 115 951 8503
email: d.hall@ihr.mrc.ac.uk

Submitted to Magnetic Resonance Imaging : 23 August 2002.

Abstract

While BOLD contrast reflects haemodynamic changes within capillaries serving neural tissue, it also has a venous component. Studies that have determined the relation of large blood vessels to the activation map indicate that veins are the source of the largest response, and the most delayed in time. It would be informative if the location of these large veins could be extracted from the properties of the functional responses, since vessels are not visible in BOLD contrast images. The present study describes a method for investigating whether measures taken from the functional response can reliably predict vein location, or at least be useful in down-weighting the venous contribution to the activation response, and illustrates this method using data from one subject. We combined fMRI at 3 Tesla with high-resolution anatomical imaging and MR venography to test whether the intrinsic properties of activation time courses corresponded to tissue type. Measures were taken from a gamma fit to the functional response. Mean magnitude showed a significant effect of tissue type ($P < 0.001$) where $\text{CSF} > \text{veins} \approx \text{grey matter} > \text{white matter}$. Mean delays displayed the same ranking across tissue types ($P < 0.001$), except that $\text{veins} > \text{grey matter}$. However, measures for all tissue types were distributed across an overlapping range. A logistic regression model correctly discriminated 72% of the veins from grey matter in the absence of independent information of macroscopic vessels ($\text{ROC} = 0.72$). Whilst tissue classification was not perfect for this subject, weighting the T contrast by the predicted probabilities materially reduced the venous component to the activation map.

Keywords : BOLD contrast, magnitude, delay, venous contribution.

Introduction

The functional MR signal is based on intrinsic BOLD (blood-oxygen-level-dependent) contrast that reflects changes in blood flow, blood volume and the relative metabolic rate of oxygen within activated cerebral tissue. Approximately 75% of the cerebral blood volume is contained in venous vessels and only 5% in the capillary bed (1, 2). Intra-cortical veins (diameters of 50 to 100 μm) resemble inverted trees where the trunks connect at right angles to pial veins (diameters of 100 to 400 μm) that run along the cortical surface and drain into the venous sinuses (3). The MR signal from within vessels is markedly affected by the paramagnetic properties of deoxygenated haemoglobin. Hence venous drainage, in intracortical and pial veins, is the dominant component of the BOLD signal, particularly at low field strength (e.g., 4). Although this venous effect becomes steeply diluted at several tens of mm distally from the neuronal activity by confluence effects (5), it may be sufficient to influence the shape and centre of mass of activation derived from statistical maps. Consequently, the true site of the cortical territory showing increased neuronal activity is likely to be contaminated by the downstream effects of these draining veins. Vascular artifacts are still present at field strengths up to 4 Tesla (6,7). This venous contribution to the MR activation signal is often overlooked in the interpretation of functional imaging data where peaks of activation (i.e. voxels that show the greatest signal change between activation and baseline states relative to their variance) are generally assumed to reflect points of highest neural activation. For accurate interpretation of fMRI data and improved localisation of function, it is desirable to separate genuine activity (that associated with the metabolic activity proximal to the capillary bed) from that of

venous drainage (that may be spatially distal to the activated tissue). However, since the neurovasculature is highly variable across subjects, the relationship between vessels and the functional activation pattern must be empirically determined for each subject.

Numerous studies at 1.5 Tesla have compared functional activation with an MR angiogram for the same subject (e.g., 1, 8-13). All these studies have involved functional activation in either the central sulcus (motor activity) or calcarine cortex (visual activity), both of which have a large draining venous system. When these functional data were correlated with a sinusoidal fit to a square wave function, generally significant voxels of high signal change and long delay were anatomically associated with large draining vessels. For example, using high resolution fMRI, Lai et al. (11) found that activation induced by finger movements precisely matched the vein in the central sulcus, rather than the grey matter tissue of the precentral gyrus. Cross-correlational analysis has also been used to determine differences in the delay of the signal between activated venous and grey matter tissue. Where delay typically refers to the time from stimulus onset to the peak in the response. The delay of the response may reflect the transit time through the vasculature, with voxels overlying draining veins having longer delays. Lee et al. (1) reported that voxels overlying pial and larger veins, as seen in the MR angiogram, had longer temporal delays than voxels anatomically associated with grey matter. Robson et al. (14) also report a positive association between the response amplitude and time to half maximum amplitude, but the response was modelled using a gamma function with a constant delay.

A significant difference between the temporal phase of the response in venous and grey matter tissue cannot always be established (e.g., 9,12). One explanation is

that the response amplitude and delay are not representative measures of the underlying activation. This case could be particularly true, where the delay is determined from the parameters of a fitted sinusoid (e.g., 9,12). The delay estimates will be unrepresentative if the activation signal does not itself strictly conform to a sinusoidal function. First, the rise and decay of the functional signal is rarely as symmetric as the sinusoid and so, in this case, the delay estimate would correspond to the peak in the curve fit rather than to the empirical peak. Second, for periods of sustained stimulation over many seconds, the magnitude of the response generally reaches a plateau or may even decrease due to neural adaptation and the nonlinearity of the haemodynamic response (e.g., 15,16). For example, for 32-s epochs, the signal approximates to a smoothed square wave rather than to a sinusoid (see Fig 3B, ref12). An appropriate curve-fitting procedure is required that generates a good fit to the stimulus response in each voxel, and thus provides satisfactory estimates of the magnitude and delay.

In the present study, we include two additional measures derived from the fit (spread and goodness-of-fit) which provide supplementary information to that of the magnitude and delay described by previous research. We used an event-related design to measure activation to a brief audio-visual stimulus. We derived voxel estimates of a series of measures from gamma density least squares fits to each average voxel timecourse. The gamma curve is asymmetric and so is appropriate for fitting positive responses that have unequal rise and decay slopes. We evaluate differences between large veins, grey matter, white matter and cerebro-spinal fluid (CSF), in terms of measures taken from the gamma fits and investigate the emergence of any general relationship between response shape and tissue type. We look beyond those activated brain areas that surround the major venous drainage systems within the central and

calcarine sulci, to include auditory activation in the temporal cortex. Our ultimate interest is in whether a combination of measures from the gamma density could provide a general basis for segregating voxels according to their neurophysiological relevance, and so permit more refined mapping. This approach is presented using a large single-subject dataset.

Materials and Methods

One healthy male subject, aged 29, was studied using a Varian 3 Tesla scanner equipped with a fast head gradient coil insert. Sets of 20 T2*-weighted EPI oblique axial brain images were acquired every 2.5 s, with a 64 by 64 image matrix, a field of view of 22.4 cm, a TE of 30 ms and a flip angle of 90°. The in-plane resolution was 3.5 x 3.5 mm, and slice thickness was 6 mm. Three further sets of image data were acquired in the same imaging plane. A 50-slice, T1-weighted structural brain image, with a voxel resolution of 1 x 1 x 3 mm, was obtained. We also acquired a 60 slice 3D, time-of-flight venous-weighted image (17) using a TE of 28 ms, and a voxel resolution of 0.4 x 0.5 x 1.9 mm. This image was weighted for BOLD contrast and optimised to visualise small veins. The third image was a B0 field map to quantify the magnetic field distortions.

Visual stimuli were projected onto a screen at the end of the scanner bed and the subject viewed the screen using prism goggles. The visual stimulus was a 6.7 Hz reversing blue and yellow checkerboard, presented for 900 ms. At the same time, pairs of spoken words were presented via high-fidelity headphones (18). The subject was requested to press a button when he heard any of three target words.

An audio-visual event occurred at each 9th TR period and within that period, it could be jittered at 5 time points, of 250, 750, 1250, 1750 and 2250 ms SOA. Thus,

the timecourse of the response to the stimulation could be reconstructed with an effective temporal resolution 500 ms across a 22.5 s time window. The response to a brief stimulus event has been shown to return to baseline within this period (19). A total of 695 sets of images were acquired giving 14 data samples for each time point in this window. For an estimation of the baseline signal, 39 sets of images were acquired at the start of the functional imaging run and 16 sets of images at the end.

Image Analysis

The magnetic field distortion map was used to refine the venous-weighted image using the FUGUE phase-unwrapping tool (20). Further post-processing of the venous-weighted image used methods described by Reichenbach et al. (21) with tools from the fMRIB software library (www.fmrib.ox.ac.uk/fsl), which masked the magnitude-contrast image by the corresponding phase-contrast image to increase visibility of small vessels, and also corrected for magnetic field nonuniformity using a homodyne demodulation reference (22).

The fMRI data were analysed using SPM99 software (<http://www.fil.ion.ucl.ac.uk/spm>). Functional images were slice-time corrected to the 10th slice and corrected for 3-D head movement. T2*- and venous-weighted images were coregistered to the T1-weighted structural image using mutual information-based registration (23). All three sets of brain images were normalised into the MNI (Montreal Neurological Institute) brain space using the structural image as a reference. The normalisation algorithm applied 7 x 8 x 7 nonlinear basis functions to correct for the geometric distortions in the T2*-weighted images relative to the T1-weighted image. Normalised images were then resampled to the same resolution (0.8 x 1.0 x 1.9 mm) using bilinear interpolation. A voxel-to-voxel correspondence was

achieved between the three image sets and the accuracy of this correspondence was verified by point-to-point visual comparison of visible landmarks across the T2*- , T1- and venous-weighted images (e.g., alignment of cortical surface, alignment of ventricles, and intra-cortical veins running within the sulci, perpendicular to the cortical surface). At this resolution, the path of cortical veins can still be visibly traced.

An event-related analysis was performed on the normalised image data, with no spatial or temporal smoothing. Low-frequency noise was removed using a 0.02 Hz high-pass filter. Variations in mean global signal intensity were not removed, because of the danger of producing spurious local changes in the direction opposite to any change in global signal. The response to each audio-visual event was modelled using a synthetic haemodynamic response function composed of two gamma functions with fixed parameters (to model the haemodynamic response with a slight undershoot) and their temporal derivatives (24). The inclusion of derivatives allows for some latitude in differential response latencies across voxels.

The T contrast for the response and its temporal derivative was computed at a corrected threshold of $T_{645} = 4.76$ ($P < 0.05$). The statistical parametric map revealed 290,834 activated voxels within numerous brain regions (21% of all brain voxels). This sample is too large for calculations based on all individual voxels. Thus, for the modelling, we included only voxels with z co-ordinates between -25 to $+42$ mm in the inferior-to-superior plane, reducing the voxel number to 193,740. This region of the brain incorporates visual and auditory regions in the occipital and temporal cortices, and excludes parts of the frontal and parietal cortices. To further reduce voxel numbers, we applied more stringent thresholding to yield a final total voxel count of 41,269. Clusters with a peak threshold of $T_{645} > 10$ and an extent > 500

identified principal activation sites. However, this statistical threshold captured many more voxels in visual cortex than in auditory cortex. Therefore, for more reliable statistical comparison with visual activation, the size of the bilateral auditory activation in the superior temporal gyrus was increased by including voxels with $T_{645} > 7$ which surrounded the auditory activation clusters that were present at $T_{645} > 10$. This approach increased the number of auditory voxels from 1,473 to 4,408. The dual statistical threshold was controlled for all subsequent statistical analyses for estimating the other variable means.

Classification of tissue type

Using the venous-weighted and the structural scans, voxels of interest were classified into four tissue types (venous, grey matter, white matter and CSF). On the basis of their different intensity characteristics, each tissue can be defined by applying an intensity filter at different cut-offs using MRIcro software (25). In the venous-weighted image, veins have a distinctively low signal due to spin dephasing and could be traced through the slice when signal intensities were filtered between -99 and -39. In the structural image, the grey matter could be segregated when signal intensities were filtered between 9603 and 14403 and the CSF between 24 and 9573. The white matter was defined by subtracting the veins, grey matter and CSF tissue from the defined regions of brain activation. An example of this classification is shown in Figure 1.

**** Figure 1 ****

Control for tissue classification error

Functional, venous-weighted and structural images were acquired at different voxel resolutions. Each functional voxel (3.5 x 3.5 x 6 mm) contained 193 voxels in the venous weighted image (0.4 x 0.5 x 1.9 mm). Thus, even after resampling all images to a resolution of 0.8 x 1 x 1.9 mm, neighbouring voxels could have a similar functional response, but a different tissue classification. Since a tissue-specific signal does not need to be as large as the voxel to materially influence its signal (due to partial volume effects), errors could be introduced in the classification of the tissue origin of each functional voxel. We logically surmise that the greater the number of adjacent voxels that share the same tissue type, the more closely is the functional voxel likely to reflect the response within that particular tissue. Tissue heterogeneity across the venous-weighted image was estimated using a measure of voxel neighbourhood. Any voxel up to 1.6, 2.0 and 3.8 mm distant on the x, y and z axes respectively was considered to be a neighbour. The more neighbours of the same tissue type that a voxel has, the more homogenous the tissue and hence the more it contributes to the estimation of the parameters of the logistic model. The number of neighbours having the same tissue classification was used as a control variable for each voxel response in all the subsequent modelling.

Gamma curve fitting to the voxel responses

For each of the 41,269 voxels, we extracted the entire signal timecourse. Weighted-mean baseline measures at the beginning and end of the time series were used to derive and subtract a linear estimate of the remaining baseline signal from each individual timecourse. Individual voxel responses to the stimulus were then reconstructed using the baseline corrected signal for a window 22.5 s following stimulus onset. For each time point in the window we have 14 data values, a mean

value was calculated on 10 data points after discarding the upper and lower two values (Figure 2). Thus, for each voxel, the mean time course is not contaminated by outliers.

**** Figure 2 ****

To estimate the measures of the response, a positive gamma curve was fitted to each representative time course. All activated voxels have a significant positive response, as the T analysis in SPM99 is directional. The gamma curve took the form of the gamma density function multiplied by a constant,

$$f(x) = c \frac{b^a}{\Gamma(a)} x^{a-1} \exp(-bx), \quad x = 0, 1, \dots, T-1 \quad (1)$$

where c is a scaling constant, x represents the data points and, a and b are the natural parameters of the gamma curve and $\Gamma(\cdot)$ is the gamma function. Gamma curves always start at the zero point ($x = 0$) and so may provide a poor fit for positive responses with a non-zero lag (i.e. voxels with a late onset response). Thus, to account for the systematic asynchrony between stimulus and response onsets, we fitted a family of gamma curves for each voxel with a range of integer post-stimulus onsets ($lag = 0, 1, 2, \dots, 9$ s), and determined the best-fitting curve by its residual sum of squares (see Figure 2). This approach to modelling variable onset time has been used previously (26,27). The fitting procedure provided convergent gamma fits for all 41,269 voxels. Transforms of the parameters for these gamma curves were taken to yield measures of delay and spread which conceptually have greater functional relevance than the natural gamma parameters (a and b). We define delay as the time, after stimulus onset, to the mean of the fitted response and it was estimated by adding the lag and the mean of the gamma function, a/b . The spread represents the temporal width of the gamma function, a/b^2 . This measure is estimated ignoring the lag. Measures of magnitude, maximum and goodness of fit (GoF) were also calculated

from the gamma curve. Magnitude is the area under the positive portion of the fitted curve (absolute magnitude > 0) and was estimated by the scaling constant c of the gamma curve, since the area of the gamma distribution (shaded area in Figure 2) is 1 by definition. The curve maximum represents the amplitude of the gamma fit when the curve reaches its peak. The maximum and magnitude measures describe similar characteristics of the gamma curve, their correlation being $r=0.95$.

A standardised GoF index Eq(2) was also obtained to enable across-voxel comparisons of how well the gamma curve summarised the functional response. In Eq(2), y_i is the mean value of the time course at time i , and \hat{y}_i is the gamma-estimated value at time i . The GoF function was weighted in a step-wise manner to give three times more importance to the goodness of fit within the initial 12.5 s (first 25 time points) of the time course, where we expect the positive response to predominantly occur, than the remainder. A low GoF index indicates a good gamma curve fit.

$$\text{GOF} = 3 * \left[\frac{\sum_{i=1}^{25} \left(y_i - \hat{y}_i \right)^2}{\sum_{i=1}^{25} \left(y_i \right)^2} \right] + \left[\frac{\sum_{i=26}^{45} \left(y_i - \hat{y}_i \right)^2}{\sum_{i=26}^{45} \left(y_i \right)^2} \right] \quad (2)$$

To determine whether the measures significantly differed across the tissue types and between the brain regions, ANOVAs were carried out on the dependent variables; magnitude, delay, spread and GoF. To provide a more robust test of the different measures, the ANOVAs controlled for the dual statistical threshold (either $7 < T < 10$ or $T > 10$) and voxel neighbourhood. The tests of magnitude, delay and spread were further controlled for GoF, since GoF indicates the reliability of these measures taken from the gamma fits.

Modelling of the gamma measures

One of the key questions is whether we can reliably discriminate between signals from underlying venous and grey matter tissue. To determine this issue, the gamma measures from just those voxels categorised as vein and grey matter tissue were included in subsequent modelling of the data. We used logistic regression (Eq[3]) which is appropriate for data with binary outcomes,

$$\log\left(\frac{p_i}{1-p_i}\right) = b_0 + b_1x_{1i} + b_2x_{2i} + \dots + b_kx_{ki} \quad (3)$$

where p_i is the probability that the i th voxel is overlying a vein (or $(1-p_i)$ is the probability of being grey matter), b_i is the coefficient and x_{1i} to x_{ki} represent the different covariates. The covariates in the logistic regression model included the magnitude, spread and delay, GoF, voxel neighbourhood, dual statistical threshold and sensory region (visual, auditory and ‘other’), plus all two-way interactions between the covariates. Again, the inclusion of GoF controlled for the low reliability of magnitude, maximum and delay estimates when the gamma curve fit was poor and voxel neighbourhood helped to control for tissue misclassification.

To discriminate between veins and grey matter tissue for the above logistic regression model, we used the receiver operating characteristic (ROC) analysis. The ROC curve is a plot of *sensitivity* (or true-positive rate) against *1-specificity* (or false positive rate). The area underneath the ROC curve serves as a well-established index of the accuracy of the logistic model and can range from 0.5 (no discrimination) to 1.0 (perfect discrimination) (28).

If the logistic regression model attains a positive discrimination ($ROC > 0.5$) between the different tissues, we can use the predicted grey matter probabilities from the model to weight the original T values from the SPM T contrast, in order to sharpen up the activation map by filtering out voxels that are less likely to be grey matter. This correction can be achieved simply by multiplying the grey matter probability of voxel, i , $(1-p_i)$ by its corresponding T value. Since the predicted probabilities vary between zero and one, all the original T values will be reduced, but the more likely that voxel, i , is classified as grey matter, the smaller will be the reduction on the T value, since $(1-p_i)$ will be closer to one. If this method is successful, then when the probability-weighted T contrast is thresholded, the ratio between the number of venous and grey matter voxels will be reduced.

Results

The event-related analysis in SPM99 ($P < 0.05$, corrected) revealed widespread activation in occipital and temporal lobes, reflecting sensory activation evoked by the audio-visual stimuli. Additional activation occurred in frontal cortex (BA4, BA6), parietal cortex (BA7, BA40) and thalamus and these areas may reflect strategy or task-related motor activity. Table 1 reports the peak locations of activation.

** Table 1 **

The defined brain region used for extracting voxel time courses excluded activated clusters in BA6, BA7 and BA40 as their z location co-ordinates exceeded +42 mm (see **Image analysis** section). The defined region included occipital cortex, temporal cortex and 'other' brain regions (predominantly the thalamus). Occipital cortex includes activation in primary visual and higher visual areas, whilst temporal

cortex includes activation in higher auditory areas. A breakdown of the numbers of voxels, split by brain region and tissue type, is given in Table 2.

**** Table 2 ****

Several of the activation clusters can be attributed to a large draining vein observed in the corresponding venous-weighted image. An example of this is illustrated in Figure 1. However, when the data are taken overall, magnitude and delay estimates for all tissue types were distributed across the same broad range (Figure 3). For the magnitude estimates, 90% lay between 559.8 and 3091.0, whilst for delay 90% lay between 4.1 and 6.2 s.

**** Figures 3 & 4 ****

ANOVA on the measures taken from the gamma curve

The mean values and confidence intervals for the four measures of interest (magnitude, delay, spread and GoF) are illustrated in Figure 4 for each tissue classification and brain region. Magnitude and spread were high in visual regions. Thus, the typical visual response could be characterised by a high peak and a broad spread across time. In contrast, auditory responses had a low magnitude, small spread and shorter delay.

For direct comparison with the literature, we first discuss magnitude and delay differences across veins and grey matter. Within visual and auditory regions, response magnitude was significantly greater in veins than in grey matter ($P < 0.05$, Bonferroni corrected). In ‘other’ regions, this difference was in the opposite direction, with grey matter having a significantly greater magnitude than veins ($P < 0.01$, Bonferroni corrected). In visual and auditory regions, delay was again longer in veins than in grey matter ($P < 0.01$, Bonferroni corrected), but there was no difference in the ‘other’

regions. Our findings in the visual and auditory cortices support the expectation that the functional response has a higher magnitude and longer delay for veins than for grey matter. The inconsistent vein/grey matter differences in ‘other’ brain regions may be influenced by the relatively poor GoF, which will make the magnitude, delay and spread measures somewhat less robust. Comparing magnitude and delay across the four tissue types, white matter had the lowest magnitude and delay, while CSF had the greatest magnitude and delay (all $P < 0.01$, Bonferroni corrected).

The most noteworthy pattern in the spread estimates was the greater spread in both visual and ‘other’ brain regions than in auditory regions ($P < 0.001$, bonferroni corrected). This pattern was also reflected in the magnitude data. The spread (temporal width of the gamma fit) and the magnitude (area under the gamma function) can be conceived as partly reflecting similar aspects of the data. Generally the GoF measures indicated acceptable curve fits, but the fits were somewhat more robust for visual and auditory regions than for ‘other’ regions ($P < 0.01$). Given that the ‘other’ regions predominantly encompass thalamic activation, one might speculate as to whether the thalamic regions are less strongly driven by the paradigm or whether the data are more noisy.

Finally, we consider differences in the measures across veins and CSF. CSF is not a source of the activation signal, but veins and CSF are often located in proximity one another, particularly where those activated regions include pial veins running along the cortical surface. Where a voxel crosses these tissue borders, signal from both veins and CSF could contribute to the response within that voxel. According to our classification, CSF contributes a smaller proportion of the voxels than veins (7.7% and 31.6% respectively). Consequently, we might expect the response measures for voxels in CSF to reflect spatial spread from their neighbours, such as adjacent veins.

This pattern may still be true even after accounting for the effects of resampling the images using the voxel neighbourhood measure of tissue homogeneity. CSF and veins were directly compared to investigate whether measures from the two tissues were similar or different. The results show a rather complex and inconsistent pattern. When the data were collapsed across brain region, magnitude and delay were higher for CSF than for veins ($P < 0.001$, Bonferroni corrected), whereas spread was equivalent across CSF and veins ($P > 0.5$, Bonferroni corrected). Thus, some gamma measures differed significantly between veins and CSF. These tissue differences indicate that the response from CSF does not completely reflect the venous response. Indeed, we were surprised to find that the effects in CSF are unlikely to be due simply to partial voluming, because CSF has a significantly longer magnitude and delay than any other tissue ($P < 0.001$). We return to this issue in the Discussion.

Discriminating veins from grey matter using logistic regression

To test whether the gamma measures could provide a robust segregation between venous tissue and grey matter, we further modelled the data using a binary logistic regression model. In summary, the covariates used in the model were the measures of magnitude, delay, spread and GoF taken from the gamma fits, the number of neighbours, plus all second-order interactions and two categorical variables (brain region and dual statistical threshold). All possible 2-way interactions were included because of plausible second-order effects among the measures. The logistic regression model converged after six iterations and a summary of the results is presented in Table 3. All the main measures of interest were significant ($P < 0.05$). Fourteen of the possible 21 interactions were also significant ($P < 0.05$). The model's discriminating power was 0.72 (ROC=0.72). Thus, the response measurements taken from the

gamma curve provided a partial, but potentially useful, discrimination between veins and grey matter.

**** Tables 3 & 4****

The vein/grey matter probabilities derived from the logistic regression model were multiplied with the SPM T contrast. For comparison with the original T contrast, the resulting probability-weighted T contrast was thresholded at $T > 7$ for auditory regions and $T > 10$ elsewhere. The probability-weighted T value of many voxels fell below this threshold (83% in fact), although fewer voxels could be eliminated by simply applying a less stringent criterion. Table 4 reports the relative numbers of venous and grey matter voxels in the thresholded statistical contrasts. For the original T contrast, the ratio between the number of venous and grey matter voxels was 0.46 for the auditory cortex and 1.00 for regions elsewhere. The vein/grey matter ratios were reduced to 0.06 and 0.38 respectively after tissue probability-weighting was applied. In both cases, this change reflects a material sharpening up of the grey matter component of the activation map.

Discussion

In this study, we derived measures of the positive functional response from gamma curve fits to the voxels' mean time course. Using a simple grey scale approach to tissue segregation, we then allocated each voxel to one of four tissue types (vein, grey matter, white matter and CSF). The range of measures taken from the gamma fits overlapped across all tissues. On average, veins had a higher magnitude and longer delay than grey matter in activated visual and auditory regions. On the basis of the measures of the functional signal, the logistic regression model did not provide an absolutely precise segregation of grey matter from venous tissue.

Nevertheless, the voxel probability values from the regression analysis provided a useful filter which reduced the proportion of venous compared with grey matter voxels in the reconstructed activation map. We report data for only a single subject, but the gains we have demonstrated by the probability-weighted T contrast would be achieved for any subject for whom a logistic regression model provides better than chance discrimination of tissue change ($\text{ROC} > 0.5$). Evidently, the discriminatory power will vary across subjects and across different stimulation paradigms.

Gamma fits

We have argued for the appropriateness of gamma curve fit for voxels activated by brief stimulus events. The gamma provides suitable constraints (e.g., single response peak) that would more robustly fit a noisy signal. The flexibility of the family of three-parameter gamma curves permitted the fitting of haemodynamic responses that varied in shape across voxels. We acknowledge that the gamma curve fits only the positive part of the haemodynamic response function, whilst ignoring the undershoot. However, given that the shape of the undershoot is highly correlated with that of the positive part (unpublished observation), it is more parsimonious and less computationally intensive to fit a unipolar function such as a gamma curve, than a bipolar function such as two gamma curves (for the positive and negative parts respectively). In general, the gamma densities are probably better than other model functions such as sinusoidal, orthogonal basis functions or splines. The sinusoid is symmetrical and would be inappropriate for this event-related study where the positive response has a short duration relative to the return to baseline. Orthogonal basis functions require the estimation of a greater number of parameters, and hence would be more computationally demanding. Splines do not have a suitable set of

constraints (i.e. they do not have to pass through zero or they do not have to rise and then fall). Furthermore, the parameters of these alternative model functions do not readily transform into physiologically meaningful variables such as maximum or delay. Nevertheless, certain caveats limit the range of experimental paradigms and research questions for which gamma curve modelling is appropriate. First, gamma fitting implicitly assumes that the response is monophasic, i.e. that there is only one positive peak per stimulus event. While the response to some long duration stimuli can be biphasic (29), this is not true for most short duration stimuli. In the present data, we did not observe any strongly biphasic responses. Second, the procedure used here for the gamma fit principally identified voxels that had a positive correlation with the stimulus since the range of the applied lags was not exhaustive. We did not seek to identify negatively correlated voxels that are highly out of phase with the stimulus. Such voxels may occur, particularly in alternating epoch study designs (12).

Overlap in response measures across tissues

Besides regional differences in the neurovascular architecture, other physiological variables (such as heart rate, blood pressure and slope of the perfusion changes) might influence the shape of the functional response, and hence the measures taken from the model fit. In particular, pressure increases at the systolic phase of the cardiac cycle cause a dynamic interaction between the competing space requirements of the blood volume, CSF and brain tissue. Large vessels exhibit pulsatile flow, but the CSF also displays pulsatility which causes an increased MR signal variance (30). A variance map for this subject showed the areas of greatest signal variance to be the movement within the eyeballs, and CSF flow within the lateral ventricles, around the cerebrum and in the fissure between the lingual gyri.

Even though low frequency components due to aliased pulsatile effects are partly removed by high pass filtering, residual variance effects may account for the difference in the response measures between CSF and other tissues. It has been argued that most of the variability in response delay occurs across spatial locations, rather than within voxels across time (12). Hence, curves were fit to estimates of a representational response delay for each voxel, thus making the assumption that each voxel response to the stimulus event was invariant over time. In this study, we focused on investigating the nature of the response variability across space rather than across time.

In the literature, the spatial variability is often attributed to large veins that drain activated areas. The contention is that delays are generally longer in veins than in other tissues, and that magnitudes are greater. For example, with respect to the delay measure, Lee et al. (1) reported that for an 18 s period of stimulation, voxels within visible vessels and sulci produced fMRI responses with 8-14 s delays, while delays in grey matter ranged from 4-8 s. These delay ranges are non-overlapping and would suggest that reasonable segregation is possible on the basis of functional measures alone. However, it is more generally found that, despite mean differences, responses from the different tissues broadly overlap (12, 31). For example, Kruggel and von Cramon (31) report a shift in the mean delay in response to single sentences across regions, but for overlapping ranges of delay. The confidence range for the delays was 5.7 to 8.3 s in left primary auditory cortex, 7.2 to 11.3 s in left superior temporal gyrus and 7.9 to 12.6 s in a midline vein complex. For comparison with the present study, in the superior temporal gyrus to presented word pairs, the response delay between veins and other tissues was significantly different, but the inter-quartile ranges overlapped (4.3 to 5.2 s in veins and 4.2 to 4.7 s in other tissues). Our delay

values are generally short because delay is directly influenced by presentation length of the stimulus. Nevertheless, our data are in close agreement with Kruggel and von Cramon's (31) evidence that not all voxels with the relatively longer delays can be mapped to large draining vessels.

Regional differences

The visual cortex appears to be much more responsive to stimulation than the auditory cortex, but greater activation could also result from a relatively high cerebral blood volume (32). Certainly from the event-related model in SPM, the maximum visual response was more than twice that in the auditory cortex (11.6% at $x = -12$, $y = -99$, $z = -15$ mm, and 5.3% at $x = 53$, $y = -36$, $z = 8$ mm respectively). There are no clear explanations as to why this should be so. The intense acoustic scanner noise could partly mask the auditory word pairs and would reduce the dynamic range available for stimulus-evoked activation. It may also be that spoken words are not the auditory equivalent of a reversing checkerboard in terms of stimulus saliency. A final contributing factor could be the non-uniformity of the blood supply throughout the brain. Although the distribution of the functional measures taken from the gamma are overlapping, all measures showed appreciable differences between visual and auditory areas that were larger than the tissue differences within each brain region. The inclusion of auditory voxels with T values between 7 and 10 increased the number of auditory voxels for modelling, but in consequence would also enhance the magnitude differences across regions because voxels with lower T scores tend to also have lower amplitude responses. However, the dual statistical cut off used was a control variable in the ANOVAs and the logistic regression. Therefore it is unlikely that the dual thresholds across regions plays an important role for the lack of tissue discrimination.

Logistic regression model

Maximum discriminability between veins and grey matter tissue was achieved by including as covariates, the set of measurements taken from the gamma fits, as well as information about each voxel's neighbourhood, dual statistical threshold and sensory region. To evaluate whether the discriminatory power could be improved by more stringent voxel selection, we recomputed the model using specific subsets of the voxels. Three criteria were investigated; the 10% of those voxels with the greatest response magnitude, the 10% of those voxels with the lowest (best) GoF, and voxels located only within the visual cortex. The area under the ROC curve was 0.72, 0.75 and 0.67 respectively. Thus, only selection by GoF improved matters, and this not materially. The high number of terms in the model contributes to the stability of its discriminatory power.

The area under the ROC showed that the model's performance was significantly greater than chance. Despite imperfect categorisation, the logistic regression model provided a useful degree of discrimination between veins and grey matter. When the predicted probabilities were used to weight the SPM T contrast, the overall number of voxels surviving the stringent T threshold reduced, but this eliminated many more voxels in venous tissue than in grey matter tissue. Thus, the probability-weighting provided more refined mapping of the non-venous activation.

The binary logistic regression model excludes the remaining CSF and white matter tissue since, by definition, there can be only two outcomes. An alternative binary logistic regression analysis could include all tissue data but categorise every voxel as grey matter or not grey matter. On the other hand, by extending the logistic

regression to the multinomial case, we can model all four tissue types explicitly and compute the probability of every voxel being grey matter. The models are otherwise similar in that the multinomial logistic regression analysis specifies the same covariates, interactions and categorical variables as the logistic regression model. For the subject reported here, the probability-weighted T contrast again showed a proportionately greater reduction of veins, CSF and white matter than the grey matter. The ratio between the number of voxels in the other three tissues (veins, CSF and white matter) and the grey matter was reduced from 1.11 to 0.29 for the auditory area, and from 2.06 to 0.56 in the visual and 'other' areas. These model results indicate that logistic regression provides a useful degree of tissue discrimination and also yields practical gains by enhancing the relative grey matter contribution to the activation map, but at a cost of also reducing the number of activated grey matter voxels.

Conclusion

Our data support the expectation that veins have a higher magnitude and a longer delay in activated sensory cortex. The statistical parameterisation of the functional time course cannot provide an absolute classification for large draining veins, but, for this subject, weighting the SPM T contrast by the probability of each tissue classification materially reduced the non-parenchymal component of the activation.

Acknowledgements

We thank Paul Matthews for providing access to the 3 Tesla MR scanner at the Oxford Centre for Functional Magnetic Resonance Imaging of the Brain and Mark Jenkinson for post-processing the venous-weighted images.

References

1. Lee AT, Glover GH, Meyer CH. Discrimination of large venous vessels in time-course spiral blood-oxygen-level-dependent magnetic resonance functional neuroimaging. *Magnetic Resonance in Medicine* 1995;**33**:745-754.
2. Sanders JA, Orrison WW. Functional magnetic resonance imaging. In : Orrison WW, Levine JD, Sanders JA, Hartshorne MF, editors. *Functional brain imaging*, St Louis: Mosby, 1995. p. 239-326.
3. Hodde KC, Sercombe, R. The anatomy of the brain vasculature. In : Mraovitch S, Sercombe R, editors. *Neurophysiological basis of cerebral blood flow control*. London: John Libbey and Co, 1996. p. 111-144.
4. Frahm J, Merbolt KD, Hänicke W, Kleinschmidt A, Boecker H. Brain or vein - oxygenation or flow? On signal physiology in functional MRI of human brain activation. *NMR in Biomedicine* 1994;**7**:45-53.
5. Turner R. BOLD localisation: The implications of vascular architecture. *NeuroImage* 2001;**13**:S1011.

6. Menon RS, Ogawa S, Tank DW, Uğurbil K. 4 Tesla gradient recalled echo characteristics of photic stimulation-induced signal changes in the human primary visual cortex. *Magnetic Resonance in Medicine* 1993;**30**:380-386.
7. Yacoub E, Shmuel A, Pfeuffer J, Van de Moortele PF, Adriany G, Andersen P, Vaughan JT, Merkle H, Ugurbil K, Hu XP. Imaging brain function in humans at 7 Tesla. *Magnetic Resonance In Medicine* 2001;**45**:588-594.
8. Haake EM, Hopkins A, Lai S, Buckley P, Friedman L, Meltzer H, Hedera P, Friedland R, Klein S, Thompson L, Detterman D, Tkach J, Lewin JS. 2D and 3D high resolution gradient echo functional imaging of the brain: venous contributions to signal in motor cortex studies. *NMR in Biomedicine* 1994;**7**:54-62.
9. Hlušík P, Noll DC, Small SL. Suppression of vascular artifacts in functional magnetic resonance images using MR angiograms. *NeuroImage* 1998;**7**: 224-231.
10. Krings T, Erberich S, Roessler F, Wurdack I, Kemeny S, Reith W, Reul J, Thon A. The “brain or vein” problem revisited- Differentiation between large draining veins and parenchymal venules in BOLD contrast fMRI. *NeuroImage* 1998;**7**:S255.
11. Lai S, Hopkins AL, Haacke EM, Li D, Wasserman BA, Buckley P, Friedman L, Meltzer H, Hedera P, Friedland R. Identification of vascular structures as a major source of signal contrast in high resolution 2D and 3D functional activation imaging of the motor cortex at 1.5T: Preliminary results. *Magnetic Resonance in Medicine* 1993;**30**:387-392.

12. Saad ZS, Ropella KM, Cox RW, DeYoe EA. Analysis and use of fMRI response delays. *Human Brain Mapping* 2001;**13**:74-93.
13. Segebarth C, Belle V, Delon C, Massarelli R, Decety J, Le BJT, Decors M, Benabid AL. Functional MRI of the human brain: Predominance of signals from extracerebral veins. *NeuroReport* 1994;**5**:813-816.
14. Robson MD, Dorosz JL, Gore JC. Measurements of the temporal fMRI response of the human auditory cortex to trains of tones. *NeuroImage* 1998;**7**:185-198.
15. Miller KL, Luh WM, Liu TT, Martinez A, Obata T, Wong EC, Frank LR, Buxton RB. Nonlinear temporal dynamics of the cerebral blood flow response. *Human Brain Mapping* 2001;**13**:1-12.
16. Vazquez AL, Noll DC. Nonlinear aspects of the BOLD response in functional MRI. *NeuroImage* 1998;**7**:108-118.
17. Reichenbach JR, Essig M, Haacke EM, Lee BC, Przetak C, Kaiser WA, Schad LR. High-resolution venography of the brain using magnetic resonance imaging. *Magnetic Resonance Materials in Biology, Physics and Medicine* 1998;**6**:62-69.
18. Palmer AR, Bullock DC, Chambers JD. A high-output, high-quality sound system for use in auditory fMRI. *NeuroImage* 1998;**7**:S359.

19. Hall DA, Summerfield AQ, Gonçalves MS, Foster JR., Palmer AR, Bowtell RW. Time-course of the auditory BOLD response to scanner noise. *Magnetic Resonance in Medicine* 2000;**43**:601-606.
20. Jenkinson, M. Improved unwarping of EPI volumes using regularised B0 maps. *NeuroImage* 2001;**13**:S165.
21. Reichenbach JR, Venkatesan R, Schillinger DJ, Kido DK, Haacke EM. Small vessels in the human brain: MR venography with deoxyhaemoglobin as an intrinsic contrast agent. *Radiology* 1997;**204**:272-277.
22. Noll DC, Nishimura DG, Macovski A. Homodyne Detection in Magnetic Resonance Imaging. *IEEE Transactions on Medical Imaging* 1991;**10**:154-163.
23. Maes F, Collignon A, Vandermeulen D, Marchal G, Suetens P. Multimodality image registration by maximization of mutual information. *IEEE Transactions on Medical Imaging* 1997;**16**:187-198.
24. Josephs O, Turner R, Friston KJ. Event related fMRI. *Human Brain Mapping* 1997;**5**:243-248.
25. Rorden C, Brett M. Stereotaxic display of brain lesions. *Behavioural Neurology* 2000;**12**:191-200.

26. Boynton GM, Engel SA, Glover GH, Heeger DJ. Linear systems analysis of functional magnetic resonance imaging in human V1. *The Journal of Neuroscience* 1996;**16**:4207-4221.
27. Buckner RL, Koutstaal W, Schacter DL, Dale AM, Rotte M, Rosen BR. Functional anatomic study of episodic retrieval II. Selective averaging of event-related fMRI trials to test the retrieval success hypothesis. *NeuroImage* 1998;**7**:163-175.
28. Thurner S, Feurstein MC, Lowen SB, Teich MC. Receiver-Operating-Characteristic Analysis Reveals Superiority of Scale-Dependent Wavelet and Spectral Measures for Assessing Cardiac Dysfunction. *Physical Review Letter* 1998;**81**:5688-91.
29. Harms MP, Melcher JR. Sound repetition rate in the human auditory pathway: Representations in the waveshape and amplitude of fMRI activation. *Journal of Neurophysiology* 2002;in press.
30. Dagli MS, Ingleholm JE, Haxby JV. Localization of cardiac-induced signal change in fMRI. *NeuroImage* 1999;**9**:407-415.
31. Kruggel F, von Cramon DY. Temporal properties of the haemodynamic response in functional MRI. *Human Brain Mapping* 1999;**8**:259-271.

32. Ogawa S, Menon RS, Tank DW, Kim SG, Merkle H, Ellermann JM, Ugurbil K. Functional brain mapping by blood oxygenation level-dependent contrast magnetic-resonance-imaging – A comparison of signal characteristics with a biophysical model. *Biophysical Journal* 1993;**64**:803-812.

Table and Figure Legends

Table 1 includes all those activated clusters with a peak voxel $T > 10$ and an extent > 500 . Activation is reported in descending value of the peak voxel statistic. Clusters above the dashed line are those included in the gamma fitting and modelling where we compare measures of the gamma curve between tissue types. Clusters below the dashed line were excluded from further analyses.

Table 2. Cross tabulation of the number of voxels in each region of the brain by tissue type. The corresponding average number of voxel neighbours is displayed in brackets. A neighbour is any voxel that is up to 1.6, 2.0 and 3.8 mm distant on the x, y and z axes respectively. The marginal values represent the column and row totals.

Table 3. Logistic regression output between venous and grey matter tissue showing all the significant main effects and interactions. The overall discriminating power of the model is 0.72. The column of β values reports each beta coefficient for the regression, where P is the corresponding p-value. The categorical variables, dual statistical threshold (T) and brain region (R), represent nominal descriptions rather than cardinal values and so a β value within each category must be set to zero to provide a 'reference' category. The reference categories selected were the threshold $T > 10$ and the auditory region.

Table 4. The table reports the number of voxels in the veins and grey matter tissue for the original and the probability-weighted T contrasts. Both T contrasts are thresholded using the same criteria, but since the threshold was region-specific the results for the

dual thresholds are shown separately. The ratio represents the quotient of the number of veins and grey matter.

Figure 1. An example of the tissue separation within an activated region of the occipital cortex. Activated voxels are shown in Panel A. Panel B denotes the activated venous tissue within this region identified from the underlying normalised venous-weighted image. Panels C, D and E show activated grey matter, white matter and cerebrospinal fluid classifications respectively and are overlaid onto the corresponding normalised structural scan. Slices are shown for the Z plane at -17 mm. The T map displayed in (A) and the venous vessel that can be traced in (B) suggest that the left-sided oblique activation cluster is associated with a large intra-cortical vein located in the calcarine and lingual sulci that drains into the sagittal sinus.

Figure 2. Schematic example of a typical functional response and its gamma fit. The response shown is for a voxel located within venous tissue at $x = 6$, $y = -100$, $z = 28$ mm. The solid line represents the mean calculated by discarding the upper and lower 20% of the values from the drift-corrected data. The dotted line represents the best gamma fit to the data. Also illustrated are the measures of delay, magnitude and lag taken from the gamma fit. The delay is represented by the time that the gamma fit takes to reach its maximum. The magnitude corresponds to the shaded area under the curve. The lag represents the number of seconds that elapses before the gamma curve fits the data.

Figure 3. Plots of the magnitude as a function of delay for the four different tissue types. The panels illustrate the striking similarity in the distribution of both the

magnitude and delay across tissues. The category for CSF contains the smallest sample of voxels, reflected by the sparser scatter plot.

Figure 4. Mean values of the magnitude, delay, spread and GoF measures displayed as a function of tissue type and brain region. The 95% confidence intervals have been corrected for multiple comparisons using a bonferroni correction procedure.

Brain region (Brodmann area)	Co-ordinates (mm)			T value
	X	Y	Z	
L lingual gyrus (18)	-12	-99	-15	23.7
R cuneus (18/19)	16	-95	34	23.6
L lingual gyrus (18)	-6	-102	2	23.4
L middle occipital gyrus (19)	-28	-98	15	20.6
R fusiform gyrus (18)	21	-87	-23	17.8
R superior temporal gyrus (22)	53	-36	8	16.0
L/R thalamus	-3	-7	6	14.3
L superior temporal gyrus (22)	-60	-57	17	14.0
.....				
L/R precuneus (7)	2	-70	68	20.8
L middle frontal gyrus (6)	-51	-4	59	18.5
R inferior parietal lobe (40)	36	-45	48	14.9
R middle frontal gyrus (6)	49	-1	61	14.8
L postcentral gyrus (7)	-30	-41	82	14.1
L/R medial frontal gyrus (6)	-3	14	55	14.0
L precentral gyrus (4)	-32	-16	82	11.7
R superior occipital gyrus (19)	22	-81	53	11.2

Table 1

	Veins	Grey Matter	White Matter	CSF	Total
Auditory	961 (13.5)	2091 (27.1)	1144 (25.0)	212 (14.3)	4408 (23.0)
Visual	11329 (22.8)	11860 (24.5)	8980 (24.8)	2832 (18.0)	35001 (23.5)
Other	727 (16.0)	210 (10.7)	803 (16.9)	120 (11.0)	1860 (15.5)
Total	13017 (21.7)	14161 (24.6)	10928 (24.3)	3179 (17.4)	41269 (23.1)

Table 2

Main Effects	β	P
R_{Auditory}	0	
R_{Visual}	-0.959	< 0.001
R_{'Other'}	3.363	< 0.001
Magnitude	1.208	< 0.001
Delay	1.206	< 0.001
Goodness of fit	-0.164	0.053
Variance	0.118	< 0.001
Neighbours	-2.759	< 0.001
T_{T > 10}	0	
T_{7 < T < 10}	-0.890	< 0.001
Interactions		
R_{Auditory} * Magnitude	0	
R_{Visual} * Magnitude	-1.178	< 0.001
R_{'Other'} * Magnitude	-2.902	< 0.001
R_{Auditory} * Delay	0	
R_{Visual} * Delay	-0.655	< 0.001
R_{'Other'} * Delay	-1.273	< 0.001
R_{Auditory} * Goodness of fit	0	
R_{Visual} * Goodness of fit	0.310	< 0.001
R_{'Other'} * Goodness of fit	-0.285	0.069
R_{Auditory} * Neighbours	0	
R_{Visual} * Neighbours	2.423	< 0.001
R_{'Other'} * Neighbours	4.726	< 0.001
T_{T > 10} * Neighbours	0	
T_{7 < T < 10} * Neighbours	0.605	0.005
Magnitude * Delay	-0.175	< 0.001
Magnitude * Variance	-0.148	< 0.001
Delay * Variance	0.080	< 0.001
Magnitude * Goodness of fit	-0.189	< 0.001
Neighbours * Variance	0.105	< 0.001
Neighbours * Goodness of fit	0.231	< 0.001
Delay * Neighbour	0.579	< 0.001
Delay * Goodness of fit	0.038	0.029

Table 3

	Vein	Grey Matter	Total	Ratio
R_{Visual & 'Other'} (T > 10)				
Original T	12056	12070	24126	1.00
Probability-weighted T	795	2106	2901	0.38
R_{Auditor} (T > 7)				
Original T	961	2091	3052	0.46
Probability-weighted T	91	1499	1590	0.06

Table 4

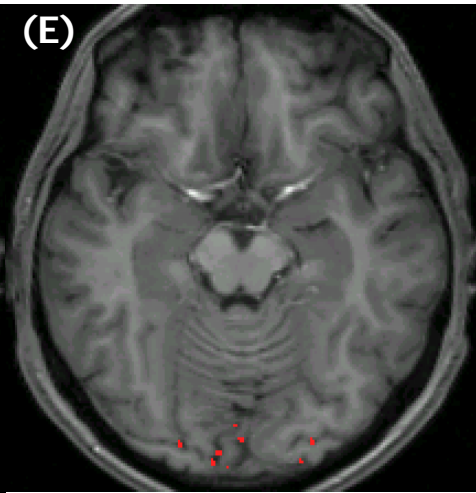
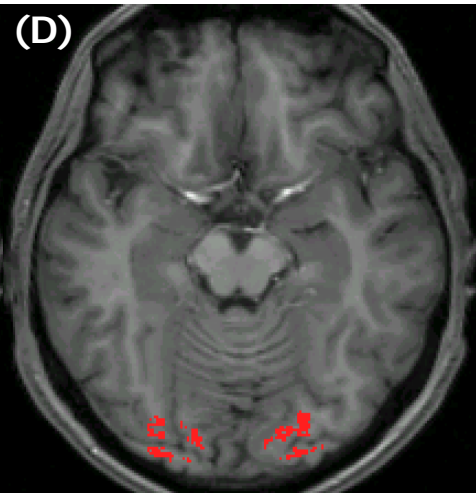
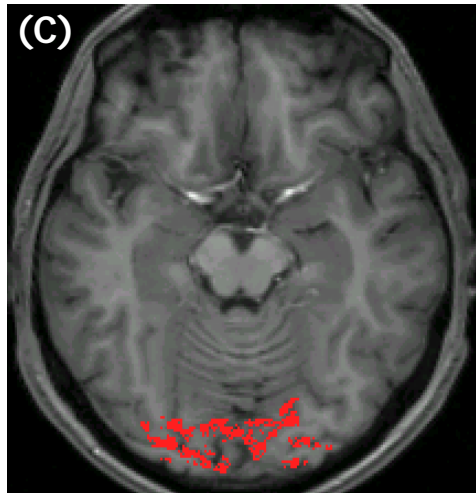
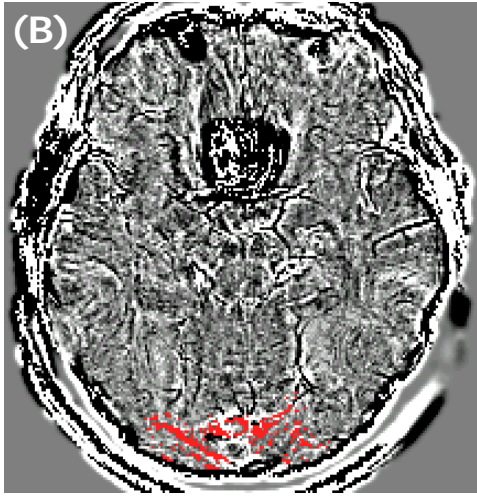
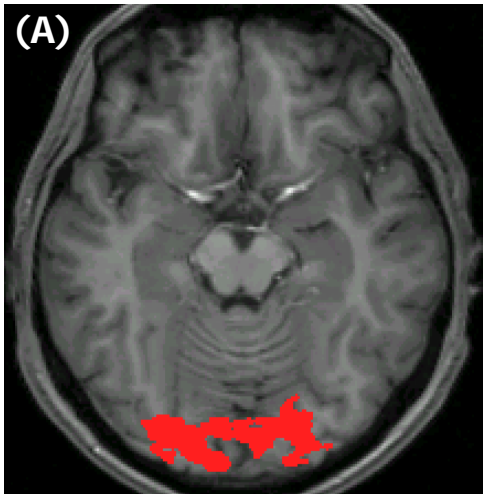


Figure 1

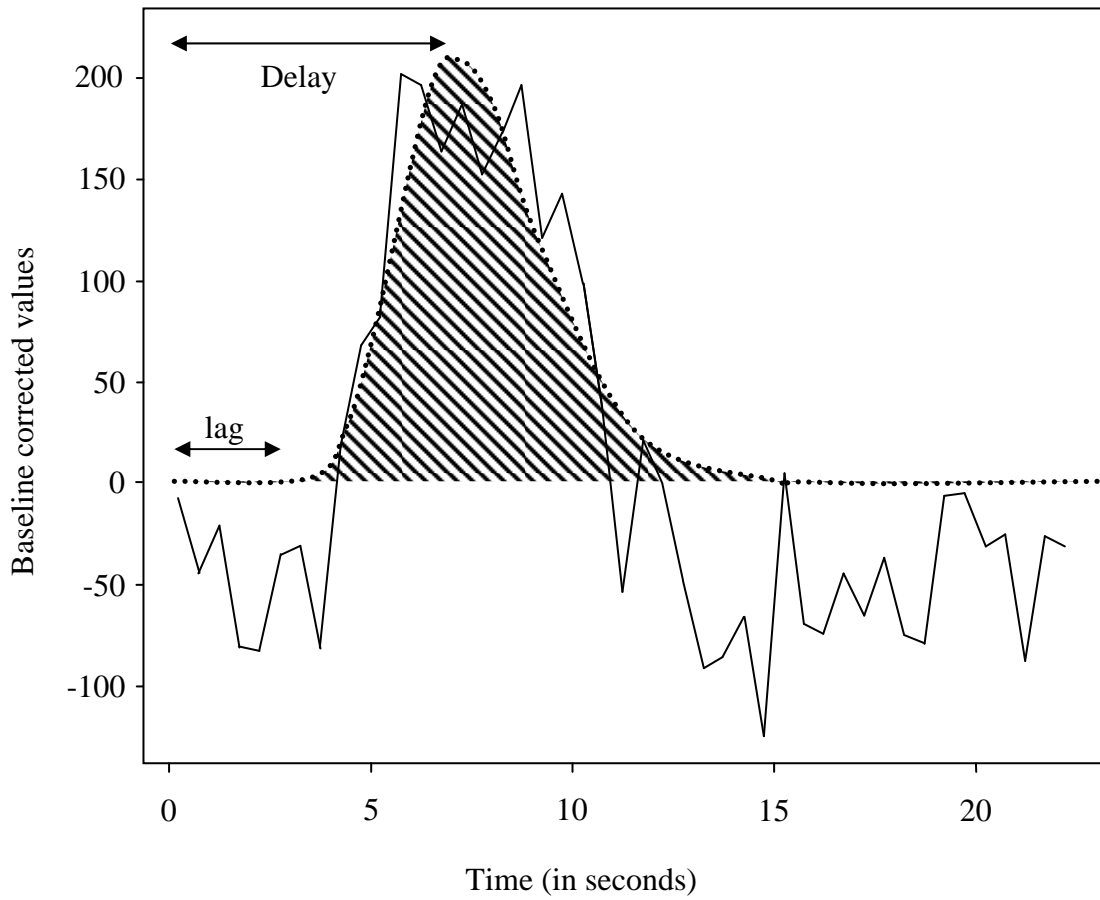


Figure 2

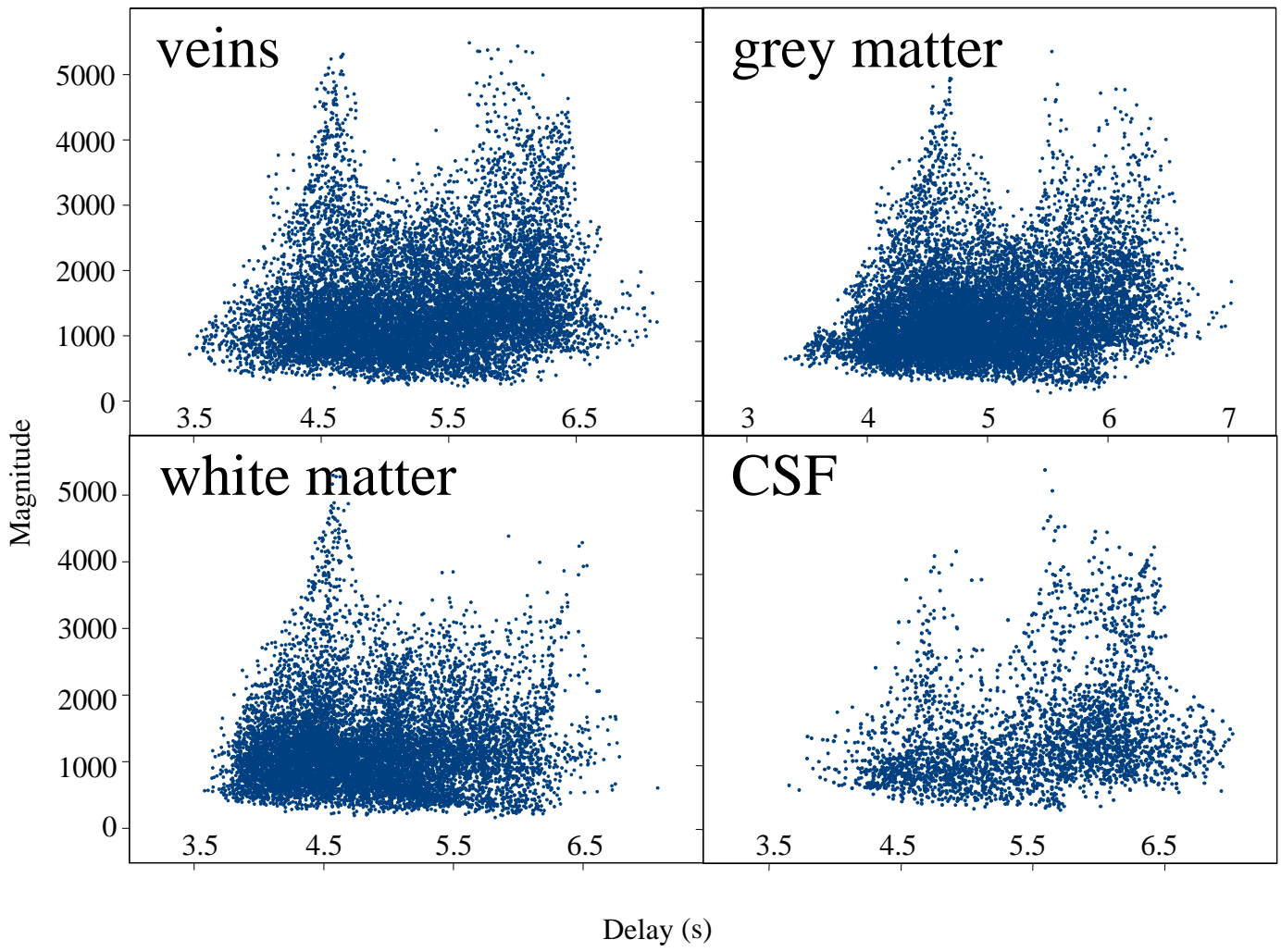


Figure 3

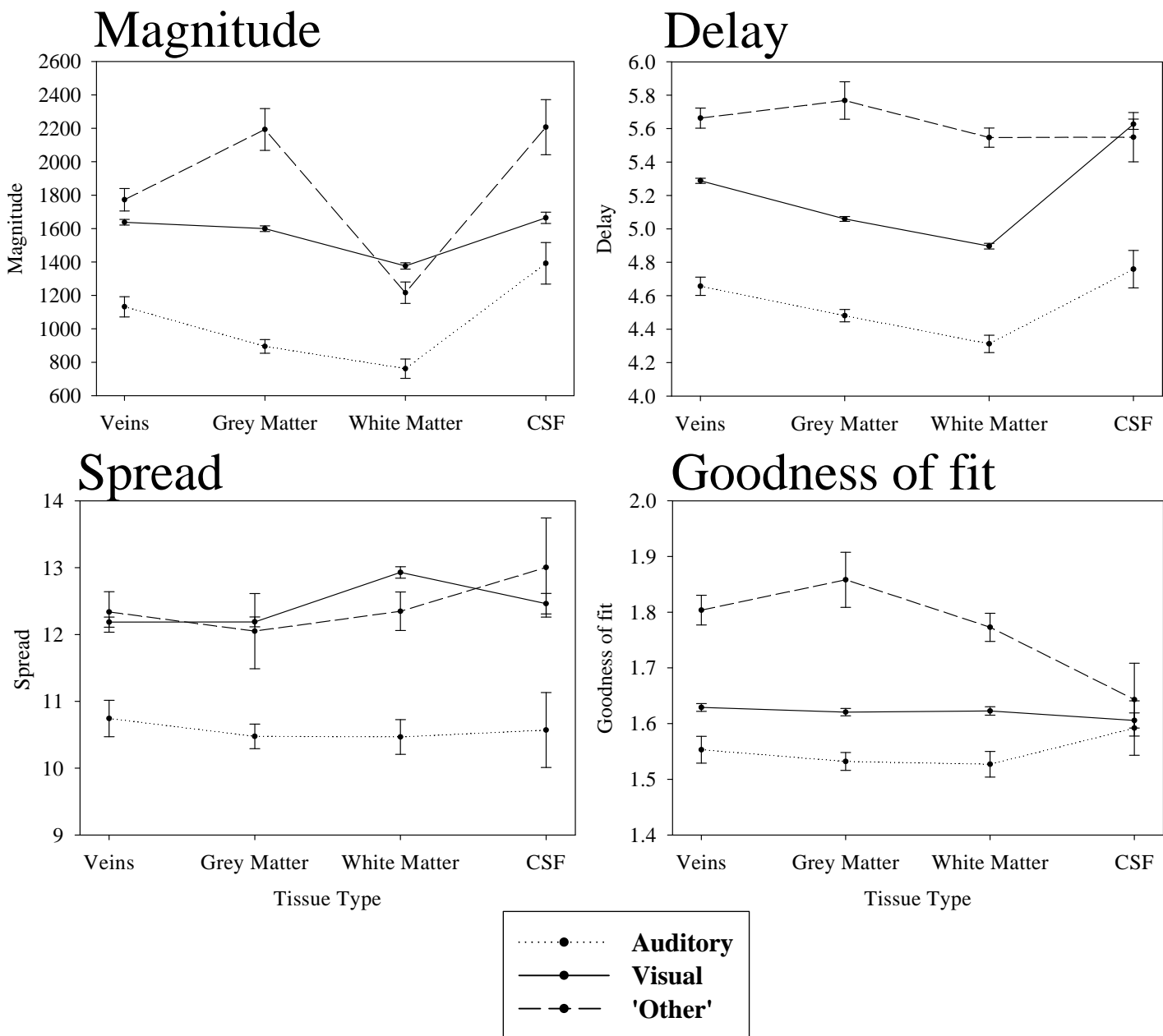


Figure 4